The Astrophysical Journal Letters, 963:L32 (8pp), 2024 March 1 https://doi.org/10.3847/2041-8213/ad2701

Backscattering of Ions Impacting Ganymede's Surface as a Source for Energetic Neutral Atoms

Paul S. Szabo[1], Andrew R. Poppe[1], Andreas Mutzke[2], Lucas Liuzzo[1], and Shane R. Carberry Mogan[1]
[1] Space Sciences Laboratory, University of California, Berkeley, 7 Gauss Way, CA 94720, USA
[2] Max Planck Institute for Plasma Physics, Wendelsteinstraße 1, 17491 Greifswald, Germany
Received 2024 January 12; revised 2024 February 5; accepted 2024 February 6; published 2024 February 29

Abstract

Jupiter's largest moon Ganymede has its own intrinsic magnetic field, which forms a magnetosphere that is embedded within Jupiter's corotating magnetospheric plasma. This scenario has been shown to lead to complex ion precipitation patterns that have been connected to heterogeneous space weathering across Ganymede's surface. We present the first simulations of energetic neutral atoms (ENAs) from backscattered H, O, and S ions, accounting for magnetospheric plasma precipitation and Ganymede's heterogeneous surface composition. Our model shows that backscattering introduces significant atomic H and O populations to Ganymede's ENA environment, which will allow remote observation of ion–surface interactions at Ganymede. There are distinct differences between H ENA emissions at Ganymede and the Moon, with orders of magnitude lower fluxes below 1 keV but a significant tail above 1 keV. Backscattered H ENAs will also dominate over sputtered H contributions above energies of around 1 keV, while O ENAs are less likely to be distinguished from sputtered ENAs. The backscattered H ENAs thus represent a promising candidate for studying the plasma–surface interaction on Ganymede with future observations of ESA's JUICE mission.

Unified Astronomy Thesaurus concepts: Ganymede (2188); Planetary magnetospheres (997); Space plasmas (1544); Planetary surfaces (2113)

1. Introduction

Ganymede is the solar system's largest moon and the only known moon with its own intrinsic magnetic field (Gurnett et al. 1996; Kivelson et al. 1996), forming a small magnetosphere within the magnetospheric plasma of its parent body Jupiter (Kivelson et al. 1997). This leads to a significant decrease of surface precipitation by the Jovian magnetospheric plasma near Ganymede's equatorial region, while much higher fluxes reach the polar regions along open field lines. This scenario has been suggested by several modeling efforts (e.g., Fatemi et al. 2016; Poppe et al. 2018; Liuzzo et al. 2020; Plainaki et al. 2020) and has been connected to the distinct color differences between low- and high-latitude regions (Johnson 1997; Cooper et al. 2001; Khurana et al. 2007), as well as recent hydrogen peroxide observations above the poles (Trumbo et al. 2023). Further plasma-induced radiolysis and erosion of the water-ice-rich surface of Ganymede are expected (e.g., Johnson et al. 2004; Teolis et al. 2017), contributing to the formation of an atmosphere, which has been studied both in observations (e.g., Barth et al. 1997; Roth et al. 2021; Leblanc et al. 2023a) and modeling (e.g., Marconi 2007; Turc et al. 2014; Leblanc et al. 2017; Vorburger et al. 2022, 2023).

The magnetosphere–surface interaction will be further studied with ESA's Jupiter Icy Moons Explorer (JUICE) mission (Grasset et al. 2013), which will orbit Ganymede as its main target at altitudes down to about 500 km. In this context, JUICE's key scientific goals will include the investigation of plasma and neutral particle environments near Ganymede. However, since the magnetospheric properties can strongly affect ion dynamics over these scales, in-situ ion measurements at JUICE's altitude will only allow limited conclusions on the actual surface precipitation of the Jovian H, O, and S ion populations (Plainaki et al. 2022). Probing the environment of energetic neutral atoms (ENAs), which are produced from ion impacts on the surface due to backscattering and sputtering, will therefore provide additional insights into the magnetosphere–surface interaction. Pontoni et al. (2022) have recently performed modeling of sputtered ENA fluxes from Ganymede to quantify them for different precipitation conditions. However, sputtered ENAs are mostly sensitive to high-energy heavy ions (Poppe et al. 2018; Pontoni et al. 2022) and are a more indirect signature of the ion impacts. In contrast, backscattered ENAs allow for a more direct measurement of the incident particle populations. While sputter yields are mostly higher than backscattering probabilities, observation opportunities arise due to the different energy and velocity distributions of backscattered and sputtered particle populations (Milillo et al. 2013).

Backscattering from planetary surfaces has so far only been observed at Earth's Moon. There, backscattered H ENAs are a prominent feature of the lunar ion–surface interaction (McComas et al. 2009; Wieser et al. 2009), dominating over sputtered ENA signatures with a backscattering probability of 0.1–0.2 (Funsten et al. 2013; Vorburger et al. 2013). The scattering has been found to depend on properties of both the incident plasma and the lunar regolith (Futaana et al. 2012; Allegrini et al. 2013; Funsten et al. 2013; Szabo et al. 2022c, 2023), allowing a remote observation of the ion fluxes that impinge on the surface (Vorburger et al. 2012; Futaana et al. 2013). Similar ENA observations are expected for ESA's BepiColombo mission, which will image the magnetosphere–surface interaction at Mercury (Lue et al. 2017; Leblanc et al. 2023b; Szabo et al. 2023). Recent progress in modeling ENA emission from backscattering at the Moon (Szabo et al. 2022c, 2023; Leblanc

Table 1
Backscattering Probabilities from SDTrimSP at Normal Incidence for Different Ion Species and Energies

	1 keV H	1 keV O	100 keV H	100 keV O	100 keV S
ice	6.2×10^{-2}	2.4×10^{-3}	2.0×10^{-4}	4.6×10^{-5}	$<2 \times 10^{-7}$
silicate	1.6×10^{-1}	2.8×10^{-2}	5.4×10^{-4}	2.2×10^{-3}	7.1×10^{-4}

Note. Backscattering probabilities for 100 keV S on ice are given as an upper limit, as no backscattering event occurred in a simulation with 5×10^6 simulated incident ions.

et al. 2023b; Verkercke et al. 2023) now allows for an extension to achieve a better description of this effect at other objects, such as Ganymede.

So far, backscattering at the Jovian moons has only been modeled for Europa (Plainaki et al. 2010, 2012). Backscattering was only considered for monoenergetic 10 keV protons while assuming the same backscattering probability as for the Moon. For Ganymede, quantitative modeling of backscattering from the surface has not yet been performed at all. We now simulate the ENA emission from backscattering with the established SDTrimSP code (Mutzke et al. 2019). In doing so, we fully account for surface precipitation fluxes from hybrid plasma simulations and estimates of Ganymede's surface composition from telescopic observations. This model approach is described in the following Section 2, after which the simulation results are presented and compared to the ENA contribution from sputtering in Section 3. Finally, the predicted backscattering features and observation opportunities for JUICE, as well as outlines for further studies are discussed in Section 4.

2. SDTrimSP Simulations of ENAs from Backscattering at Ganymede

H backscattering simulations are performed with SDTrimSP version 7.0 (Mutzke et al. 2019; see Appendix A for more details), using the graphical user interface from Szabo et al. (2022a). With a regolith-grain implementation in SDTrimSP-3D (Von Toussaint et al. 2017), we previously modeled ENA emission due to backscattering of solar wind protons from the lunar surface in agreement with Chandrayaan-1 and IBEX ENA measurements (Szabo et al. 2022c, 2023). These studies showed that the main regolith-related effects are reduced backscattering probabilities under oblique incidence and backwards-dominated scattering angle distributions, while energies of backscattered ENAs are similar to a flat surface. Therefore, we consider backscattering from a flat surface under normal incidence as a reasonable approximation for the first studies of ion impacts on Ganymede, as we mainly aim to provide an estimate of backscattered fluxes and their energy spectra in the present work.

For the present study, we assume the surface composition of Ganymede as a mixture of H_2O ice and hydrated silicate minerals to account for Ganymede's partial coverage with water ice (Kieffer & Smythe 1974; Calvin et al. 1995; Hansen & McCord 2004; Ligier et al. 2019; King & Fletcher 2022; Bockelee-Morvan et al. 2024). Serpentines have been proposed as dark surface material on the Galilean moons (Calvin & Clark 1991) and we choose $(Mg,Fe)_3(Si_2O_5)(OH)_4$ with an Mg:Fe ratio of 2:1 for the nonice surface component. Table 1 gives an overview of backscattering probabilities for 1 keV H and O, as well as 100 keV H, O, and S ions at normal incidence using both an ice and a serpentine surface. Modeled backscattering probabilities from ice are consistently significantly lower than those from silicates or those observed at the Moon (Funsten et al. 2013; Vorburger et al. 2013). Wieser et al. (2016) experimentally found higher backscattering probabilities of 0.28 for 1 keV H from ice, but their experiments were performed at a grazing incidence angle of 83° to the surface normal. This represents a highly favorable irradiation geometry for backscattering and at this angle, SDTrimSP even gives a backscattering probability of 0.63 for 1 keV H from a flat ice surface, compared to 6.2×10^{-2} for normal incidence (see Table 1). Due to the incidence and emission angles of 83° in the experiments by Wieser et al. (2016), it is reasonable to expect a strong scattering in the forward direction into the instrument. However, the significant roughness of the ice sample reduces the backscattering probability for oblique incidence compared to a flat surface (Szabo et al. 2022c; Verkercke et al. 2023), likely explaining the discrepancy in backscattering probabilities between simulation and laboratory experiment.

3. Results

3.1. Backscattered H ENA from Different Regions on Ganymede's Surface

To study backscattered ENA fluxes at Ganymede, we use the energy spectra of precipitating ions from previously published hybrid plasma simulations and energetic particle tracing for H^+, O^+, O^{2+}, and S^{3+} ions (Fatemi et al. 2016; Poppe et al. 2018). A clear shielding of the trailing hemisphere equatorial region was found, while precipitation onto the surface is much more favorable along the open field lines over the polar regions and Ganymede's magnetic cusps. Trailing hemisphere cusp regions especially favor lower energy (about 1 keV) thermal H and O fluxes.

Following this behavior, we separate Ganymede's surface into three regions of interest for modeling backscattered ENAs: (1) high-latitude regions, (2) cusp regions, and (3) low-latitude regions. The cusp regions correspond to the location of the open-closed-field line boundary (Duling et al. 2022) and follow the main precipitation of thermal H ions (see Appendix B). For each of the regions, we determine the average ice and silicate abundances from the composition maps by Ligier et al. (2019): 59% ice for the high-latitude regions, 39% for the cusp regions, and 24% for the low-latitude region.

Dashed lines in Figure 1 show the differential fluxes for H precipitation as a function of energy for the three regions. Thermal H fluxes in the cusps are about 1 order of magnitude higher than over the high-latitude regions (at least for energies below a few keV), while the precipitation onto the low-latitude part of Ganymede's surface decreases by 2 to 3 orders of magnitude across all energies. Figure 1 also depicts our SDTrimSP simulation results of H backscattering as solid lines. Furthermore, a typical lunar ENA spectrum in the form of the Maxwell–Boltzmann fit from Futaana et al. (2012) is included

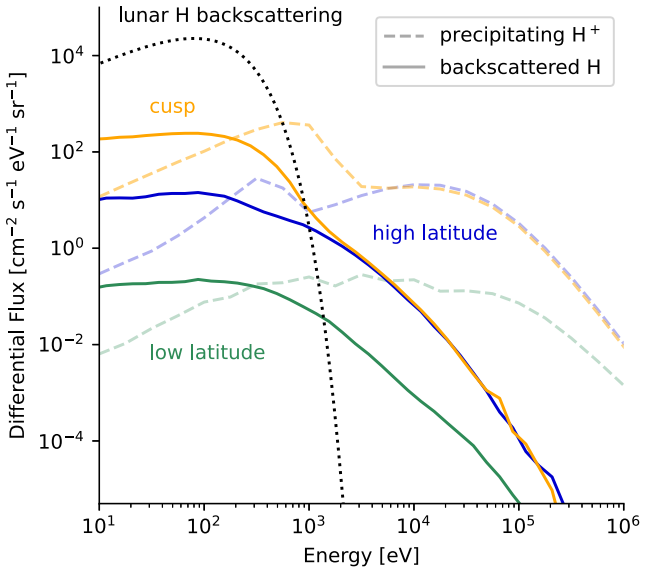

Figure 1. Backscattered H ENA fluxes from the three regions of Ganymede's surface (solid lines) are compared to the respective precipitation fluxes (dashed lines) and a typical spectrum of lunar backscattered ENAs from Futaana et al. (2012; dotted line).

as the black dotted line. The characteristic decrease of the ENA flux above a few 100 eV that is observed in lunar ENA energy spectra is similarly seen for Ganymede, while the flux below this energy is predicted to be several orders of magnitude lower than at the Moon. However, an extended high-energy tail occurs for backscattering from Ganymede due to the energetic H^+ ions in the precipitating spectrum. Details of the backscattered H ENA spectra greatly vary for the three different regions: the lower energy component of the cusp ENA flux is more than 1 order of magnitude higher than for the high-latitude region corresponding to the increased peak precipitation flux there. Energy spectra of backscattered ENAs from the equatorial regions are similar in shape to those from the poles, but almost 2 orders of magnitude lower in flux. All these variations are similar in both precipitating and backscattered fluxes, showing how properties of the former are reproduced in the latter populations.

3.2. ENA Contribution from Backscattering Compared to Sputtering

In order to assess the contribution of H backscattering to Ganymede's ENA environment, we compare our simulation results to the sputtered ENA fluxes modeled by Pontoni et al. (2022). In their study, Pontoni et al. (2022) consider sputtered ENAs in the form of H_2O, H_2, and O_2. JUICE's ENA instruments have mass-resolving capabilities, but atomic H ENAs can also be formed in the likely dissociation of H_2O and H_2 molecules in the instrument (Wieser et al. 2016). These H ENAs would have less energy than the original molecules, as each H only transports energy corresponding to its mass fraction of the molecular mass ($1/18$ for H_2O and $1/2$ for H_2; see Appendix C for more details).

We compare fluxes of backscattered H ENAs to those from dissociated sputtered species, respectively, averaged over Ganymede's entire surface in Figure 2(a). We include backscattered spectra for three different ice/silicate abundances with ice concentrations of 10%, 35%, and 65%, which encompass the whole range of ice abundances reported by Ligier et al. (2019). The sputtering contributions are included as the dashed lines for the same surface compositions. In this context, we neglect any sputtering from silicates due to significantly lower yields than for ice (see, e.g., Famá et al. 2008; Johnson et al. 2009; Szabo et al. 2018, 2020a). Thus, we account for surface composition by multiplying the H ENA fluxes from sputtering by the fraction of ice at the surface. Figure 2(b) further gives the relative contribution to the total ENA flux from backscattering at different energies for the three surface compositions. Generally, H ENAs from backscattering contribute significantly to the total H ENA signal above energies of 100 eV, especially for low ice abundances. For the high-energy tail in the keV region and above, backscattering then becomes the dominant H ENA contribution irrespective of surface composition.

Most of the contribution to the sputtered fluxes shown with the dashed line comes from H_2. However, H_2 emission at energies of tens of eV or higher will be unlikely if H_2 is preferentially removed from the surface thermally as suggested by Teolis et al. (2009, 2017). This could lead to an energy distribution of emitted H_2 that is dominated by a thermal component with much lower energies than 10 eV, the lower bound of the energy range of JUICE's Jovian Neutral Atoms Analyzer instrument. In contrast, the Thompson–Sigmund collisional sputtering distribution assumed by Pontoni et al. (2022) favors higher emission energies. Thus, we also include the sputtering contribution without H_2 as the dotted line, which causes it to be significantly reduced. In this case, the backscattered ENAs dominate over the sputtered ENA signal above 100 eV for all compositions.

3.3. Backscattered O and S ENAs

Given the high precipitation fluxes of thermal O^+ ions, we also model the formation of O ENAs from the backscattering of thermal and energetic O populations. Figure 3(a) gives an overview of the results in the same manner as was done for H in Figure 2(a). Backscattered O ENAs are compared to O from the dissociation of sputtered H_2O and O_2, with the H_2O contribution being dominant. Overall, the results are similar to those for H as backscattered O ENAs contribute noticeably to the total predicted ENA signal above around 100 eV. However, our simulated O backscattering fluxes are much more similar to the sputtered fluxes over the whole energy range than was the case for H. This is due to O ions having a smaller backscattering probability than H as well as only small changes in the sputtered energy spectra from dissociation.

For the globally averaged flux at an ice concentration of 35%, Figure 3(b) compares the differential backscattered fluxes for H, O, and S. The higher precipitating flux of thermal O ions compensates for the lower backscattering probability, causing the O differential flux spectrum to be very similar to the H spectrum when plotted over energy. Backscattered S fluxes from the purely energetic ion population are significantly lower than those of H and O. Even at ENA energies of several keV or tens of keV, their contribution to the ENA environment will be minor.

4. Discussion

4.1. Comparison to Backscattered ENAs at the Moon

Previous observations and modeling of solar wind backscattering from the lunar surface have shown that the ENA

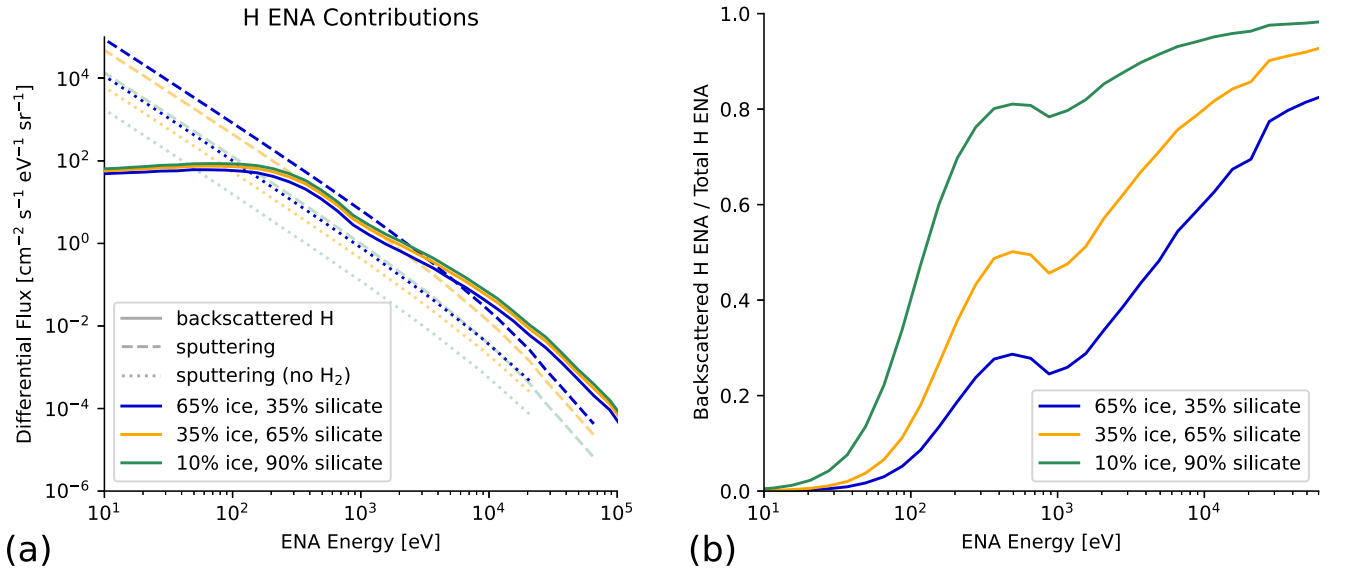

Figure 2. (a) Globally averaged backscattered H ENA fluxes (solid lines) are compared to the sputtered atomic ENA fluxes (from dissociation in an ENA instrument, dashed lines, based on the calculations by Pontoni et al. 2022) at three different ice abundances. Given uncertainties in the emission of high-energy H_2, the dotted line depicts sputtered fluxes with the H_2 component excluded. (b) The relative contribution of backscattered H ENAs to the total H ENA environment (backscattered + sputtered, including the H_2 component) is plotted based on the data shown in (a).

emission depends on the properties of both the precipitating ions and the surface (e.g., Futaana et al. 2012; Funsten et al. 2013; Vorburger et al. 2013; Szabo et al. 2022c, 2023; Leblanc et al. 2023b; Verkercke et al. 2023). With the above-described simulations, we have extended the SDTrimSP modeling of backscattering from the Moon to Ganymede accounting for magnetospheric ion precipitation and an ice/silicate mixture composition of the surface. This leads to key differences compared to lunar ENA spectra.

Our simulation results suggest that reflection probabilities from Ganymede for H are significantly smaller than for the Moon, where 0.1–0.2 have been reported (Funsten et al. 2013; Vorburger et al. 2013; Szabo et al. 2023). This is related to both the ice-rich surface composition and the higher ion impact energies at Ganymede. With the reported ice abundances for Ganymede from Ligier et al. (2019), this gives proton backscattering probabilities of 7.5×10^{-3} for the high-latitude regions, 5.1×10^{-2} for the cusps, and 7.9×10^{-3} for the low-latitude region. These lower values together with lower precipitation fluxes compared to the Moon, ultimately give backscattered ENA spectra in the 10^1–10^3 eV range (corresponding to the ENAs that can be measured by instruments such as Chandrayaan-1's CENA and JUICE's JNA) that are at least about 2 orders of magnitude lower than observed at the Moon (Wieser et al. 2009; Futaana et al. 2012). The general trend of the H ENA differential flux of almost constant values at low energies and a decrease above a few 100 eV is observed for Ganymede as well. This can be related to the thermal H ions, whose differential flux is predicted to peak at energies similar to solar wind protons. However, the backscattered H ENA energy spectrum at Ganymede possesses a high-energy tail beyond 1 keV corresponding to the backscattering of the energetic H ion population. This high-energy tail represents a distinct difference from backscattered ENAs at the Moon and provides an observation opportunity for backscattering with JUICE's Jovian Energetic Neutrals and Ions (JENI) instrument.

In contrast to the Moon, Ganymede's surface is also exposed to significant fluxes of O^+ and O^{2+} ions over a broad energy range (Plainaki et al. 2015; Clark et al. 2016; Poppe et al. 2018), with backscattering probabilities between 9.3×10^{-3} and 2.1×10^{-2} for the global average. High precipitation fluxes of the thermal O ions also lead to our model results suggesting similar O ENA fluxes and H ENA fluxes. It can thus be expected that both backscattered H and O provide significant contributions to Ganymede's ENA environment. For energetic S ions, precipitating fluxes and especially backscattering probabilities are much lower (2.7×10^{-4}–6.9×10^{-4} for the Ganymede-relevant range of ice abundances, with backscattering essentially only occurring from the silicate component of the surface).

4.2. Backscattering Contributions to the ENA Environment of Ganymede

Our comparison with the sputtering model from Pontoni et al. (2022) shows that the JNA instrument (energy range 10 eV–3.3 keV) should mainly observe backscattered ENAs above energies of around 1 keV and over regions of lower ice abundances. For the JENI instrument that is capable of measuring H at energies above about 0.5–1 keV (Mitchell et al. 2016), backscattering will give a larger ENA contribution than sputtering. This will likely not hold for backscattered O because of higher fluxes of sputtered H_2O. Distinct observation of backscattered H will thus be easier to achieve than that of backscattered O.

However, the comparison between ENA contributions from backscattering and sputtering is significantly affected by uncertainties in the assumptions for the energies of sputtered species. Sputtering as a result of a collision cascade can typically be well described with a Thompson–Sigmund distribution that decreases with $1/E^2$ for large energies E (Behrisch & Eckstein 2007; Jäggi et al. 2023). Pontoni et al. (2022) use this assumption for all of their sputtered fluxes irrespective of sputtered species and impactor energies. This becomes increasingly uncertain for electronic sputtering at high impact energies (several keV and above for H; about 10 keV and above for O and S; Baragiola et al. 2013; Johnson et al. 2013), representing

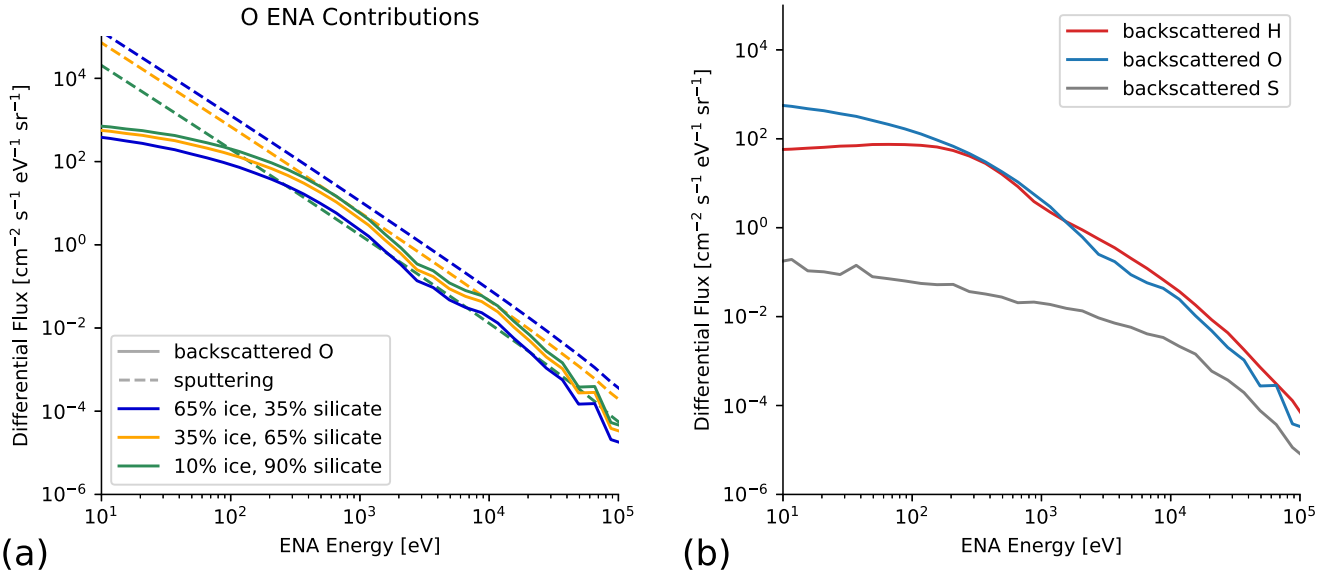

Figure 3. (a) In the same manner as in Figure 2(a), backscattered O fluxes are compared to the ENA contribution from sputtered H_2O. (b) For a globally averaged precipitation flux and an ice surface concentration of 35%, backscattered ENA fluxes for H, O, and S are shown.

the major contributor to sputtering of icy surfaces on Ganymede (Pontoni et al. 2022). In this regime, sputtering is not the result of direct nuclear collisions, but of ion-induced excitations that are converted into kinetic energy (Behrisch & Eckstein 2007). Laboratory experiments suggest a combination of a thermal distribution and a $1/E^2$ tail (Brown et al. 1984; Haring et al. 1984; Pedrys et al. 2000; Johnson et al. 2013; Vorburger et al. 2022). However, the sputtered energies have only been reported up to about 10 eV and it remains to be studied how effective electronic sputtering is at producing ENAs of 100–1000 s of eV. This holds especially for H_2, which likely thermally diffuses out of the surface before it can be sputtered (Teolis et al. 2009). Furthermore, the energies relevant to JUICE's ENA measurements are mostly significantly higher than the dissociation energy of H_2O (O–H bond energy of about 5 eV; Maksyutenko et al. 2006), so that interatomic collision energy transfer on the order of 100–1000 s of eV should be very efficient in releasing dissociated atomic products from the surface rather than molecular H_2O. Thus, the total composition of sputtered products at low energies could be different than that at high energies.

Wieser et al. (2016) do observe significant ENA signals from sputtering up to keV energies, but this could also be affected by the grazing-incidence irradiation geometry used in that study. Under such oblique incidence, direct knock-on sputtering is much more likely to occur than in geometries closer to normal incidence. Taking these knowledge gaps into account, there is significant potential for further studies on the sputtering behavior of water ice, specifically focusing on the energy distributions of different sputtered species and the effect of varying incidence angles on these distributions, to better understand the ENA populations that will be observed by JUICE.

Another potential ENA source that could contribute at keV energies and above is the charge exchange of gyrating ions with Ganymede's atmosphere. Haynes et al. (2023) have recently discussed this effect for Callisto and Europa, showing fluxes on the order of $10^0\,\mathrm{cm^{-2}\,s^{-1}\,sr^{-1}\,eV^{-1}}$ for energy ranges of 1–100 keV. These fluxes are higher than those of backscattered ENAs at the same energies, but significant differences in these moons' local magnetic topologies indicate that future studies should focus specifically on Ganymede before a quantitative comparison is made.

5. Conclusions

We present the first modeling of backscattered ENA emission from the surface of Ganymede, showing how this process will contribute to the neutral atom environment there. Our simulations show that Ganymede's H ENA spectra from backscattering are similar in shape but orders of magnitude lower in flux than ENA emission from the Moon up to about 1 keV. For Ganymede, there also exists a high-energy H ENA tail due to the backscattering of energetic ions, which will likely dominate over any sputtered H ENAs independent of surface composition. Due to the high O precipitation, similar fluxes of backscattered H ENAs and O ENAs can be expected to occur. However, it will be difficult to distinguish backscattered O from sputtered H_2O in future JUICE measurements. Thus, atomic H represents the most promising ENA species for studying Ganymede's magnetosphere–surface interaction.

Until JUICE reaches the Jovian system and starts orbiting Ganymede in close proximity, several further studies to better understand ENA formation as a result of the plasma–surface interaction should be aimed for. On one hand, extended backscattering measurements using icy surfaces and Ganymede-relevant energies would provide additional validation for the SDTrimSP simulation approach. Future sputtering experiments for characterizing high-energy ENA emission at hundreds of eV and above would help distinguish different ENA-forming processes at the Galilean moons and any other icy bodies. On the other hand, global plasma simulations that take into account recent Juno observations of the ion environment near Ganymede will also be helpful to establish improved local precipitation of Ganymede's surface (Paranicas et al. 2021; Allegrini et al. 2022; Clark et al. 2022; Hansen et al. 2022).

Acknowledgments

The authors gratefully acknowledge support from NASA's Solar System Research Virtual Institute (SSERVI) via the LEADER team, grant 80NSSC20M0060.

Data Availability

The research data presented in this manuscript are included in the accompanying data set uploaded to Zenodo (Szabo et al. 2024). Licenses of SDTrimSP can be acquired by contacting sdtrimsp@ipp.mpg.de or the Max-Planck-Innovation GmbH. The SDTrimSP graphical user interface is available on github (https://github.com/psszabo/SDTrimSP-GUI; Szabo et al. 2022b).

Appendix A
SDTrimSP Simulations

A.1. Model Parameters

Similar to previous ENA studies (Szabo et al. 2022c, 2023), we use a KrC screened Coulomb interaction potential in our SDTrimSP simulations. We also employ default stopping power settings (stopping power model inel0 = 4 for H and inel0 = 7 for O and S). Several other interatomic potentials and stopping power models were tested, with none having a significant effect on the simulation outcomes.

Past publications have also discussed the use of different surface binding energies in SDTrimSP (see, e.g., Szabo et al. 2020b; Morrissey et al. 2022; Jäggi et al. 2023; Morrissey et al. 2023), but the surface binding energy is a more important parameter for sputtering rather than backscattering due to the lower emission energies of sputtered atoms. We apply the surface binding energy model isbv = 2 (weighted average) with default surface binding energies for water ice, and with an increased O binding for the silicate minerals, as described in Szabo et al. (2020b).

Figures A1–A3 present examples for parameter tests, which demonstrate the limited sensitivity of the simulation results to different inputs. This especially holds when uncertainties in the precipitation flux inputs are taken into account.

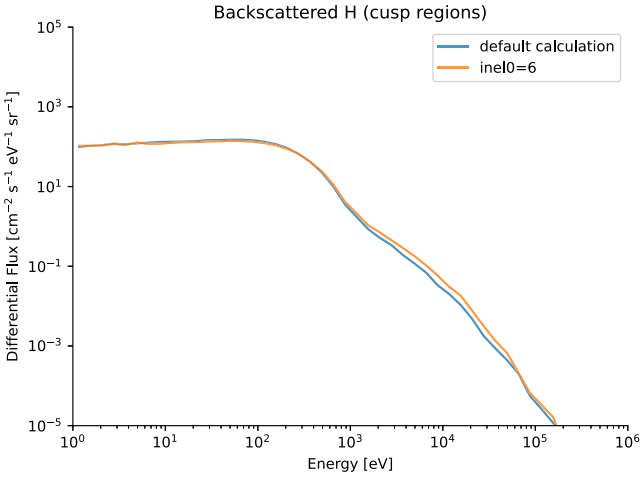

Figure A1. Different SDTrimSP simulations of H scattering from water ice for cusp region precipitation fluxes. The default simulation is done with the stopping model parameter inel0 = 4.

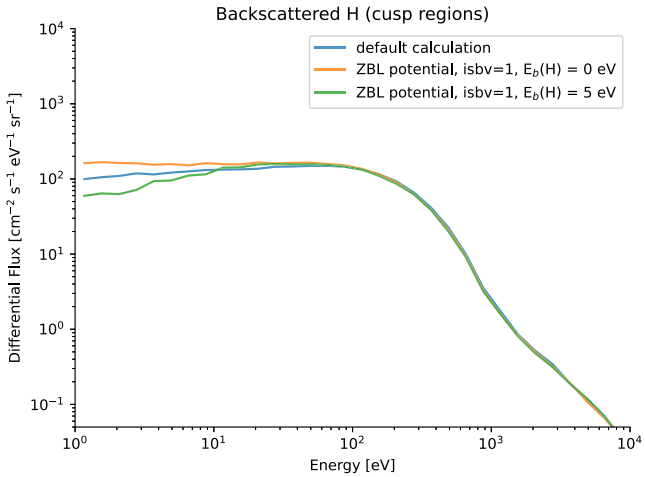

Figure A2. Same as Figure A1, but focused on interatomic potentials and surface binding energy models. The default simulation is done with a KrC potential and the averaged surface binding model isbv = 2, resulting in a surface binding energy $E_b = 1.59$ eV for the H projectile in the simulation.

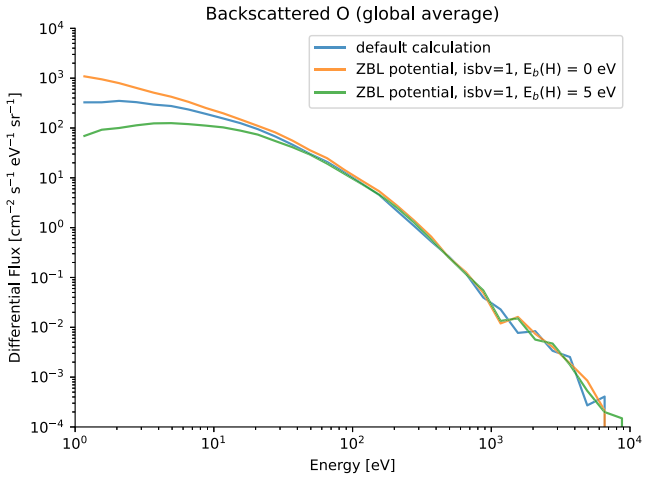

Figure A3. Different SDTrimSP simulations of O scattering from water ice for precipitation conditions that are averaged over the whole surface of Ganymede. The default simulations use a KrC potential and isbv = 2, giving $E_b = 1.59$ for the O projectile in ice.

A.2. Neutralization of Backscattered Particles

SDTrimSP is not able to account for the charge states of impinging ions and model the neutralization process. As was also done for previous lunar studies (Szabo et al. 2022c, 2023), we therefore assume that all backscattered particles are reflected from the surface as ENAs, based on the generally very low observed fraction of backscattered protons at the Moon (Lue et al. 2018).

Appendix B
Regions of Ganymede's Surface

We empirically define the cusp regions as 25° latitude wide stripes along the following lines of $|\theta_{\rm lat}| = \sin(\phi_{\rm lon} - 180^\circ) \cdot 15^\circ + 47^\circ$, with latitudes $\theta_{\rm lat}$ and W longitudes $\phi_{\rm lon}$.

The cusp regions correspond to the location of the open-closed-field line boundary (Duling et al. 2022) and follow the location of the main precipitation of thermal H ions (see Figure B1(a)). For each of the regions, we determine the ice and silicate abundances from the composition maps from the study

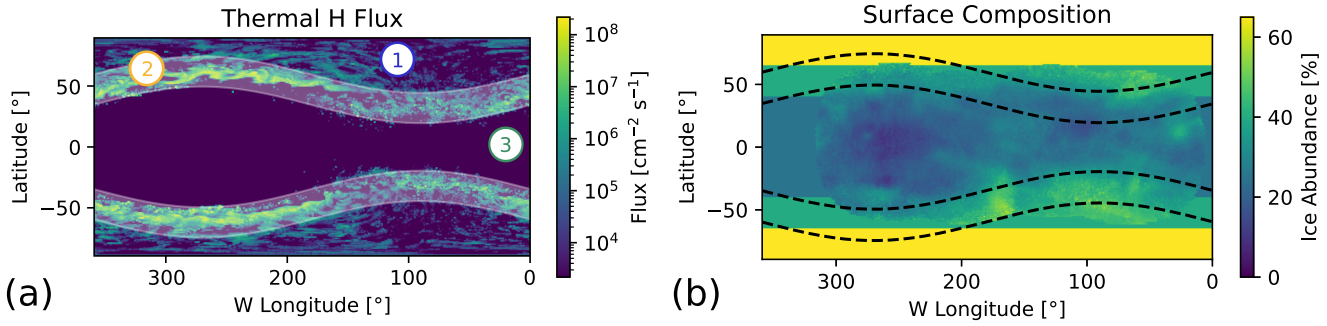

Figure B1. (a) Following the different regimes of thermal H precipitation flux from Poppe et al. (2018), we separate Ganymede's surface into three regions of interest: (1) high-latitude regions, (2) cusp regions, and (3) low-latitude regions. (b) The different regions are largely associated with different ice abundances on the surface. Ice abundance maps are from Ligier et al. (2019) with estimates for the edges from Vorburger et al. (2022).

by Ligier et al. (2019; addended with filled-in average values in Vorburger et al. 2022, see Figure B1(b)). We derive average surface compositions of 59% ice for the high-latitude regions, 39% for the cusp regions, and 24% for the low-latitude region.

Appendix C
H ENAs from Dissociation of H_2 and H_2O in an ENA Instrument

Pontoni et al. (2022) modeled the sputtering of H_2O, H_2, and O_2, showing that ENAs in the high-energy tail of the sputtered distributions could be used to observe surface precipitation with JUICE. Thus, sputtering from water ice mostly provides molecular ENAs, while backscattering produces atomic ENAs. However, the JNA and JENI ENA instruments onboard JUICE require scattering from a charge conversion surface or passing through a foil for their measurements. Both of these interaction processes are likely to cause dissociation of the molecule in the instrument, making it harder to distinguish molecular from atomic species. The prediction of JNA count rates due to sputtered ENAs by Pontoni et al. (2022) did not explicitly include this, but dissociation was stated as "most likely" to occur. Wieser et al. (2016) reported a H signal following oxygen ion bombardment in their JNA calibration that was attributed to an energy-dependent dissociation efficiency of sputtered H_2O in the instrument.

For comparing backscattered and sputtered ENA contributions, we assume that every sputtered H_2O and H_2 dissociates in the instrument to give an upper limit for sputtered ENAs that would be registered in the same mass channels as backscattered, atomic ENAs. The dissociation would also cause a change in registered energy as each atom only carries a part of the energy of the molecule corresponding to the ratio of the atom's mass to the molecule's mass ($1/18$ for H from H_2O and $1/2$ for H from H_2). At the same time, both H_2O and H_2 break up into two atomic H, ultimately causing an increase of the measured signal as well as a shift to lower energies.

The measured H ENA flux from sputtering $f_H^{\text{meas.}}$ thus becomes a sum of contributions from dissociation of H_2O and H_2:

$$f_H^{\text{meas.}}(E)dE = 36 f_{H_2O}^{\text{sputt.}}(18E)dE + 4 f_{H_2}^{\text{sputt.}}(2E)dE. \quad \text{(C1)}$$

The factors 36 and 4 stem from both a factor 2 due to the number of H atoms in each molecule and factors 18 and 2, respectively, that have to be applied to conserve the total integral $\int f(E)dE$. As the energy decreases, the flux per energy interval increases. Due to the significant energy shift for H from H_2O dissociation and the steep decrease of $1/E^2$ of the Thompson–Sigmund energy distribution assumed by Pontoni et al. (2022) for all sputtered molecules, $f_H^{\text{meas.}}$ still becomes dominated by the H_2 contribution.

ORCID iDs

Paul S. Szabo https://orcid.org/0000-0002-7478-7999
Andrew R. Poppe https://orcid.org/0000-0001-8137-8176
Andreas Mutzke https://orcid.org/0000-0003-0517-6817
Lucas Liuzzo https://orcid.org/0000-0002-4820-8594
Shane R. Carberry Mogan https://orcid.org/0000-0002-0261-8117

References

Allegrini, F., Dayeh, M., Desai, M., et al. 2013, P&SS, 85, 232
Allegrini, F., Bagenal, F., Ebert, R., et al. 2022, GeoRL, 49, e2022GL098682
Baragiola, R., Famá, M., Loeffler, M., et al. 2013, The Science of Solar System Ices, Vol. 527 (New York, NY: Springer), 527
Barth, C., Hord, C., Stewart, A., et al. 1997, GeoRL, 24, 2147
Bockelee-Morvan, D., Lellouch, E., Poch, O., et al. 2024, A&A, 681, A27
Behrisch, R., & Eckstein, W. 2007, in Sputtering by Particle Bombardment: Experiments and Computer Calculations from Threshold to MeV Energies, 110, ed. R. Behrisch & W. Eckstein (Berlin: Springer)
Brown, W., Augustyniak, W., Marcantonio, K., et al. 1984, NIMPA, 1, 307
Calvin, W. M., & Clark, R. N. 1991, Icar, 89, 305
Calvin, W. M., Clark, R. N., Brown, R. H., & Spencer, J. R. 1995, JGRE, 100, 19041
Clark, G., Mauk, B., Paranicas, C., Kollmann, P., & Smith, H. 2016, JGRA, 121, 2264
Clark, G., Kollmann, P., Mauk, B., et al. 2022, GeoRL, 49, e2022GL098572
Cooper, J. F., Johnson, R. E., Mauk, B. H., Garrett, H. B., & Gehrels, N. 2001, Icar, 149, 133
Duling, S., Saur, J., Clark, G., et al. 2022, GeoRL, 49, e2022GL101688
Famá, M., Shi, J., & Baragiola, R. 2008, SurSc, 602, 156
Fatemi, S., Poppe, A., Khurana, K., Holmström, M., & Delory, G. 2016, GeoRL, 43, 4745
Funsten, H., Allegrini, F., Bochsler, P., et al. 2013, JGRE, 118, 292
Futaana, Y., Barabash, S., Wieser, M., et al. 2013, GeoRL, 40, 262
Futaana, Y., Barabash, S., Wieser, M., et al. 2012, JGRE, 117, E05005
Grasset, O., Dougherty, M., Coustenis, A., et al. 2013, P&SS, 78, 1
Gurnett, D., Kurth, W., Roux, A., Bolton, S., & Kennel, C. 1996, Natur, 384, 535
Hansen, C., Bolton, S., Sulaiman, A., et al. 2022, GeoRL, 49, e2022GL099285
Hansen, G. B., & McCord, T. B. 2004, JGRE, 109, E01012
Haring, R., Pedrys, R., Oostra, D., Haring, A., & De Vries, A. 1984, NIMPB, 5, 483
Haynes, C. M., Tippens, T., Addison, P., et al. 2023, JGRA, 128, e2023JA031931
Johnson, R. 1997, Icar, 128, 469
Johnson, R., Burger, M., Cassidy, T., et al. 2009, Europa (Tucson, AZ: Univ. of Arizona Press), 507
Johnson, R., Carlson, R., Cooper, J., et al. 2004, Jupiter: The Planet, Satellites and Magnetosphere, 1 (Cambridge: Cambridge Univ. Press), 485

Johnson, R. E., Carlson, R. W., Cassidy, T. A., & Fama, M. 2013, The Science of Solar System Ices (New York: Springer), 551
Jäggi, N., Mutzke, A., Biber, H., et al. 2023, PSJ, 4, 86
Khurana, K. K., Pappalardo, R. T., Murphy, N., & Denk, T. 2007, Icar, 191, 193
Kieffer, H. H., & Smythe, W. 1974, Icar, 21, 506
King, O., & Fletcher, L. N. 2022, JGRE, 127, e2022JE007323
Kivelson, M., Khurana, K., Russell, C., et al. 1996, Natur, 384, 537
Kivelson, M. G., Khurana, K., Coroniti, F., et al. 1997, GeoRL, 24, 2155
Leblanc, F., Oza, A. V., Leclercq, L., et al. 2017, Icar, 293, 185
Leblanc, F., Roth, L., Chaufray, J.-Y., et al. 2023a, Icar, 399, 115557
Leblanc, F., Deborde, R., Tramontina, D., et al. 2023b, P&SS, 229, 105660
Ligier, N., Paranicas, C., Carter, J., et al. 2019, Icar, 333, 496
Liuzzo, L., Poppe, A. R., Paranicas, C., et al. 2020, JGRA, 125, e28347
Lue, C., Futaana, Y., Barabash, S., et al. 2017, Icar, 296, 39
Lue, C., Halekas, J., Poppe, A. R., & McFadden, J. 2018, JGRA, 123, 5289
Maksyutenko, P., Rizzo, T. R., & Boyarkin, O. V. 2006, JChPh, 125, 181101
Marconi, M. 2007, Icar, 190, 155
McComas, D., Allegrini, F., Bochsler, P., et al. 2009, GeoRL, 36, L12104
Milillo, A., Orsini, S., Plainaki, C., et al. 2013, P&SS, 88, 53
Mitchell, D., Brandt, P., Westlake, J., et al. 2016, JGRA, 121, 8804
Morrissey, L. S., Schaible, M. J., Tucker, O. J., et al. 2023, PSJ, 4, 67
Morrissey, L. S., Tucker, O. J., Killen, R. M., Nakhla, S., & Savin, D. W. 2022, ApJL, 925, L6
Mutzke, A., Schneider, R., Eckstein, W., et al. 2019, IPP-Report, SDTrimSP Version 6.00, https://pure.mpg.de/rest/items/item_3026474/component/file_3028154/content
Paranicas, C., Szalay, J., Mauk, B., et al. 2021, GeoRL, 48, e2021GL093021
Pedrys, R., Krok, F., Leskiewicz, P., et al. 2000, NIMPB, 164, 861
Plainaki, C., Massetti, S., Jia, X., et al. 2022, ApJ, 940, 186
Plainaki, C., Milillo, A., Mura, A., Orsini, S., & Cassidy, T. 2010, Icar, 210, 385
Plainaki, C., Milillo, A., Mura, A., et al. 2012, Icar, 218, 956
Plainaki, C., Milillo, A., Massetti, S., et al. 2015, Icar, 245, 306
Plainaki, C., Massetti, S., Jia, X., et al. 2020, ApJ, 900, 74
Pontoni, A., Shimoyama, M., Futaana, Y., et al. 2022, JGRA, 127, e2021JA029439
Poppe, A., Fatemi, S., & Khurana, K. 2018, JGRA, 123, 4614
Roth, L., Ivchenko, N., Gladstone, G. R., et al. 2021, NatAs, 5, 1043
Szabo, P., Poppe, A., Mutzke, A., et al. 2023, JGRE, 128, e2023JE007911
Szabo, P., Poppe, A., Mutzke, A., Liuzzo, L., & Carberry Mogan, S. 2024, Backscattering of Ions Impacting Ganymede's Surface as a Source for Energetic Neutral Atoms (Dataset), v1.0, Zenodo, doi:10.5281/zenodo.10480937
Szabo, P. S., Weichselbaum, D., Biber, H., et al. 2022a, NIMPB, 522, 47
Szabo, P. S., Weichselbaum, D., Biber, H., et al. 2022b, SDTrimSP GUI (Software), v1.0, Zenodo, doi:10.5281/zenodo.10622330
Szabo, P. S., Chiba, R., Biber, H., et al. 2018, Icar, 314, 98
Szabo, P. S., Biber, H., Jäggi, N., et al. 2020a, JGRE, 125, e2020JE006583
Szabo, P. S., Biber, H., Jäggi, N., et al. 2020b, ApJ, 891, 100
Szabo, P. S., Poppe, A. R., Biber, H., et al. 2022c, GeoRL, 49, e2022GL101232
Teolis, B., Plainaki, C., Cassidy, T., & Raut, U. 2017, JGRE, 122, 1996
Teolis, B., Shi, J., & Baragiola, R. 2009, JChPh, 130, 134704
Trumbo, S. K., Brown, M. E., Bockelée-Morvan, D., et al. 2023, SciA, 9, eadg3724
Turc, L., Leclercq, L., Leblanc, F., Modolo, R., & Chaufray, J.-Y. 2014, Icar, 229, 157
Verkercke, S., Chaufray, J.-Y., Leblanc, F., et al. 2023, PSJ, 4, 197
Von Toussaint, U., Mutzke, A., & Manhard, A. 2017, PhST, 2017, 014056
Vorburger, A., Fatemi, S., Carberry Mogan, S. R., et al. 2023, Icar, 409, 115847
Vorburger, A., Fatemi, S., Galli, A., et al. 2022, Icar, 375, 114810
Vorburger, A., Wurz, P., Barabash, S., et al. 2012, JGRA, 117, A07208
Vorburger, A., Wurz, P., Barabash, S., et al. 2013, JGRA, 118, 3937
Wieser, M., Futaana, Y., Barabash, S., & Wurz, P. 2016, Icar, 269, 91
Wieser, M., Barabash, S., Futaana, Y., et al. 2009, P&SS, 57, 2132